Characterization of the beamstrahlung radiation at the future high-energy circular collider

Manuela Boscolo and Andrea Ciarma[*]
INFN - Laboratori Nazionali di Frascati, Via Enrico Fermi, 54, 00044 Frascati RM, Italy

(Received 27 July 2023; accepted 5 October 2023; published 9 November 2023)

Beamstrahlung is a dominant effect in the beam dynamics of the high luminosity next-generation lepton collider FCC-ee. We characterize the beamstrahlung radiation for the beam parameters at the four working energies, from the Z-pole to the $t\bar{t}$ threshold, and present the effect of this radiation in the machine-detector-interface region. We discuss the conceptual need for a photon dump due to the high power produced, which is in the order of hundreds of kilowatts. We also discuss the detector induced backgrounds due to the incoherent e^+e^- pairs produced by the interaction of the beamstrahlung photons at the interaction point.

DOI: 10.1103/PhysRevAccelBeams.26.111002

I. INTRODUCTION

Future high-energy circular colliders like FCC-ee [1] maximize their luminosity by squeezing the bunches at the interaction point (IP) to nanobeam scales, and by pushing the number of particles per bunch to the limit allowed by the beam-beam interaction. Due to the highly-dense bunches at the IP, the synchrotron radiation emitted during the collision in the electromagnetic field of the opposing beam, known as beamstrahlung (BS) [2], is very intense. This effect has been known since 1978 from early studies of multi-TeV lepton colliders [3] and was broadly studied in preparation for the SLC [4,5]. Whenever a particle traverses the opposing bunch at the IP, it will radiate and may lose sufficient energy to fall below the momentum acceptance, or contribute to the formation of the high-energy tails and increase of the beam energy spread. The beamstrahlung radiation is collinear to the beam, emitted in a cone of aperture about $1/\gamma$.

We used the generator GuineaPig++ [6] to simulate the single beam-beam interaction including the production of beamstrahlung radiation. This radiation was then tracked through the detector using Key4HEP [7] to evaluate the induced backgrounds. The paper is organized as follows. In Sec. II we introduce the beamstrahlung process in itself with no reference to lattice versions or specific simulations but through the beamstrahlung parameter for the FCC-ee case; in Sec. III we discuss the properties of the beamstrahlung radiation with simulation results for a precise set of beam parameters and optics for FCC-ee; in Sec. IV we introduce the first concept study for handling this intense radiation; in Sec. V we show the dependence of the beamstrahlung radiation on the beam parameters by comparing two different FCC-ee optics. Section VI presents the radiation produced by radiative Bhabha, with the aim of comparing it with that from beamstrahlung, shown in Sec. III; in Sec. VII we describe the induced backgrounds coming from the e^+e^- pairs produced by the beamstrahlung photons, and finally in Sec. VIII we give few concluding remarks.

II. BEAMSTRAHLUNG RADIATION

The strength of the BS radiation is characterized by the dimensionless beamstrahlung parameter Υ [4], defined as

$$\Upsilon = \frac{2}{3}\frac{\hbar\omega_c}{E}, \tag{1}$$

where E is the particle energy before the radiation emission and $\hbar\omega_c = \frac{3}{2}\frac{\hbar c\gamma^3}{\rho}$ is the critical energy E_{crit} [8] for a particle with curvature radius ρ. Each bunch particle experiences a different beam-beam force depending on its position in the 6D phase space, and it also varies during the crossing of the opposing bunch, so the BS parameter Υ is not constant during the collision. The maximum and average values Υ_{max} and Υ_{avg} [4] are used to describe the global behavior of the two colliding bunches. For head-on collisions of Gaussian bunches these values are defined as:

$$\Upsilon_{\mathrm{ave}} \sim \frac{5}{6}\frac{r_e^2\gamma N_e}{\alpha\sigma_z(\sigma_x^* + \sigma_y^*)} \qquad \Upsilon_{\mathrm{max}} = \frac{12}{5}\Upsilon_{\mathrm{ave}}, \tag{2}$$

where α is the fine structure constant, r_e the electron classical radius, γ the Lorentz factor, N_e the bunch population, $\sigma_{x,y}^*$ the rms bunch dimensions at the collision

---

[*] Corresponding author: andrea.ciarma@lnf.infn.it

TABLE I. Relevant parameters for the BS description for various circular and linear e^+e^- colliders.

	E (GeV)	N_e (10^{10})	σ_x^* (μm)	σ_y^* (nm)	σ_z (mm)	Υ_{ave} (1)
FCCee Z-pole	45.6	17	6.4	28	12.1	175×10^{-6}
FCCee $t\bar{t}$	182.5	23	38.2	68	2.54	760×10^{-6}
SuperKEKB e^-	7	9.04	10.1	48	6	18×10^{-6}
SuperKEKB e^+	4	6.53	10.7	62	5	86×10^{-6}
SLC	50	4	2.1	900	1.1	0.00152
ILC	250	2	0.64	5.7	0.3	0.0456
CLIC	165	0.52	0.149	2.9	0.07	0.144
CLIC 3 TeV	1500	0.37	0.045	1.0	0.044	4.91
NLC	1000	1.1	0.36	2.3	0.1	0.535

point, and σ_z the longitudinal bunch length. It appears from Eq. (2) that Υ is linearly proportional to the beam energy, and to the bunch density. For FCC-ee it has been found in simulations [9] that the BS has a strong effect on the beam lifetime and luminosity, being the main driver for the energy spread and bunch length. The derivation of the equilibrium emittances and bunch length in presence of BS for lepton circular colliders is described in [10], resulting in agreement with the numerical simulations performed so far [11]. At the FCC-ee Z-pole the equilibrium bunch length and energy spread are increased by about a factor three with respect to the noncolliding bunches (i.e., dominated by the synchrotron radiation only) [12].

Table I reports Υ_{ave} evaluated using Eq. (2) for various circular and linear e^+e^- colliders [13–17]. For circular colliders the equilibrium beam parameters have been considered.

At FCC-ee $\Upsilon_{\mathrm{ave}} \ll 1$ and beams are flat, as $\sigma_y/\sigma_x \ll 1$. Under these conditions the particle average energy loss δ_E [10] can be expressed as a function of Υ_{ave}:

$$\delta_E = \frac{16\sqrt{3}}{5\pi^{3/2}} \frac{r_e \alpha N_e}{\sigma_x^*} \Upsilon_{\mathrm{ave}} = \frac{24}{3\sqrt{3}\pi^{3/2}} \frac{r_e^3 \gamma N_e^2}{\sigma_z \sigma_x^{*2}}. \tag{3}$$

The average number of photons emitted per particle, n_γ, and their average energy, $\langle E_\gamma \rangle$, can be evaluated according to [10]:

$$n_\gamma = \frac{12}{\pi^{3/2}} \frac{\alpha^2 \sigma_z}{r_e \gamma} \frac{6}{5} \Upsilon_{\mathrm{ave}} = \frac{12}{\pi^{3/2}} \frac{\alpha r_e N_e}{\sigma_x^*}, \tag{4}$$

$$\langle E_\gamma \rangle = \frac{\delta_E}{n_\gamma} E_e = \frac{4\sqrt{3}}{15} \Upsilon_{\mathrm{ave}} E_e. \tag{5}$$

Equations (3), (4), and (5) indicate the dependence of the bunch density on the BS effect.

FCC-ee adopts the crab-waist collision scheme [18] that requires a large Piwinski angle, defined by $\Phi = \sigma_z/\sigma_x^* \tan(\theta/2)$, where θ is the horizontal crossing angle. This scheme modifies the effective length of the interaction area, which can be defined as:

$$L_i = \frac{\sigma_z}{\sqrt{1 + \Phi^2}}. \tag{6}$$

For Piwinski angles above $\Phi \geq 1$, L_i is smaller and not comparable with the bunch length. In this case Eqs. (3) and (4) become [19]:

$$n_\gamma = \frac{12}{\pi^{3/2}} \frac{\alpha r_e N_e}{\sigma_x^*} \frac{1}{\sqrt{1 + \Phi^2}}, \tag{7}$$

$$\delta_E = \frac{24}{3\sqrt{3}\pi^{3/2}} \frac{r_e^3 \gamma N_e^2}{\sigma_z \sigma_x^{*2}} \frac{1}{\sqrt{1 + \Phi^2}}. \tag{8}$$

III. BEAMSTRAHLUNG RADIATION POWER AND DIVERGENCE

We characterized the BS radiation at FCC-ee with GuineaPig++ simulations of single collisions, referring to the beam parameters for optics version labeled v530 as shown in Table II. In GuineaPig++ the Gaussian beams are cut longitudinally in slices and transversely in cells, and are populated with macroparticles. Bunch crossing is simulated by shifting slices, and the force on each macroparticle is calculated using the charge distributed in the cells of the opposite beam [6]. The beams are assumed Gaussian because we are interested in estimating the total power emitted via this process, so photons emitted by particles outside the core have a negligible contribution. We considered for our simulations the equilibrium beam sizes, at nominal current and in collision.

In the last two rows of Table II we list the resulting total power and the mean energy of the produced BS photons, obtained from GuineaPig++ simulations. The highest power value is about 400 kW and is observed at the Z-pole due to the high current at this energy. The average radiation energy is highest at the $t\bar{t}$, as expected also from Eq. (3). Photon mean energies range from 2 to 63 MeV, with tails of few hundreds of MeV at the Z-pole and up to few GeV at the $t\bar{t}$ threshold. The peak photon flux goes from 10^{12} to 10^{14} photons per second 0.1% bandwidth, growing with the beam current (higher at the Z-pole working point).

TABLE II. Beam parameters for the FCC-ee 4 IP lattice v530 as from Ref. [12]. The index SR refers to the single beam equilibrium parameters in presence of synchrotron radiation only, the index BS refers to the collision case, with beamstrahlung. The last two rows indicate the total power and mean energy of the beamstrahlung radiation, as obtained from GuineaPig simulations.

Parameter	Units	Z	WW	ZH	$t\bar{t}$
Beam energy	GeV	45.6	80.0	120.0	182.5
Horizontal emittance ϵ_x	nm rad	0.71	2.16	0.64	1.49
Vertical emittance ϵ_y	pm rad	1.42	4.32	1.29	2.98
Horizontal IP β_x	m	0.1	0.2	0.3	1
Vertical IP β_y	mm	0.8	1	1	1.6
Horizontal IP beam size σ_x^*	μm	8.46	20.78	13.86	38.60
Vertical IP beam size σ_y^*	nm	33.7	65.7	35.9	69.0
Bunch length σ_z (SR/BS)	mm	4.38/15.4	3.55/8.01	3.34/6.0	2.00/2.74
Momentum spread σ_δ (SR/BS)	%	0.038/0.132	0.069/0.154	0.103/0.185	0.157/0.221
Bunch population N_e	10^{11}	2.43	2.91	2.04	2.37
Bunches/beam n_b		10 000	880	248	40
BS total power	kW	370	250	150	80
BS mean energy $\langle E_\gamma \rangle$	MeV	2	7	23	63

These results are in very good agreement with the first estimates discussed in Refs. [20,21].

The flux of the BS photons per unit of bandwidth as a function of their energy at the four working points is shown in Fig. 1.

This intense and energetic photon flux requires to be properly handled. We discuss in the following the first estimates to evaluate the photon spot size and divergence, necessary to establish possible locations of the BS dump in the tunnel. These evaluations have been used to consider the feasibility of an extraction photon beam line for a dump at few hundreds meters from the IP.

Table III reports the photon and electron beam divergences, which result comparable, as expected. The photon angular spread goes from about 45 μrad at the $t\bar{t}$ threshold to about 92 μrad at the Z-pole. These values correspond to a photon beam spot of about 1 cm^2 at 100 m downstream the collision point at the Z-pole, and about 0.5 cm^2 at the $t\bar{t}$ threshold.

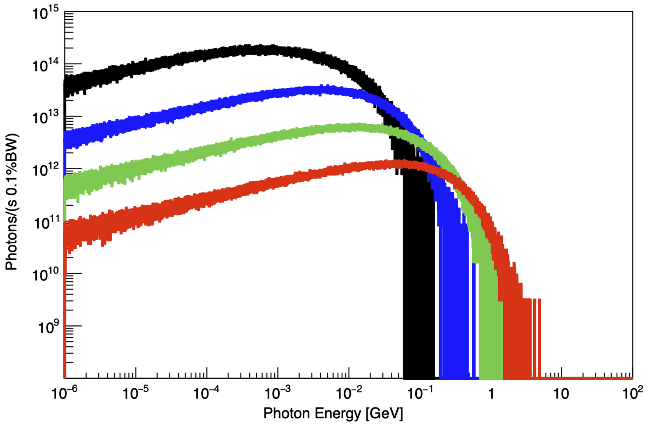

FIG. 1. Flux of the BS radiation as a function of their energy, emitted for the four FCC-ee working points, 45.6 GeV (black), 80.0 GeV (blue), 120.0 GeV (green), and 182.5 GeV (red).

Figure 2 shows the horizontal and vertical angular distributions of the BS radiation at the four FCC-ee working points. On the horizontal direction, photons receive a net kick due to the asymmetry induced by the crossing angle. The radiation emitted at higher energies has the center of the distribution closer to the longitudinal beam axis (corresponding to zero in the plot) because higher energy particles are more rigid and curve less in a magnetic field, according to the definition of beam rigidity

$$B\rho = P/0.3, \tag{9}$$

where $P[\mathrm{GeV}/c]$ is the particle momentum, $B[T]$ the magnetic field and $\rho[m]$ the bending radius. The same does not happen in the vertical plane, as there is no preferential direction induced by the charge spatial distribution, so the photon vertical angular distributions are centered at zero.

The difference between the values of $\langle p_x \rangle$ at the lowest and highest energies (Z-pole and $t\bar{t}$ threshold) is 35 μrad. Comparing these values with the photon angular divergences in Table III, it can be observed that this offset is small enough to assure that the cores of the distributions are still broadly overlapped, as appears in Fig. 2.

TABLE III. Divergence of the photon and electron beams.

	$\sigma_{\theta_x}(\gamma)$ (μrad)	$\sigma_{p_x}(e^-)$ (μrad)	$\sigma_{\theta_y}(\gamma)$ (μrad)	$\sigma_{p_y}(e^-)$ (μrad)
Z	91.8	84.3	49.2	42.1
WW	110	103.4	73.0	65.7
ZH	51.7	46.2	41.3	35.9
$t\bar{t}$	44.6	38.6	50.3	43.2

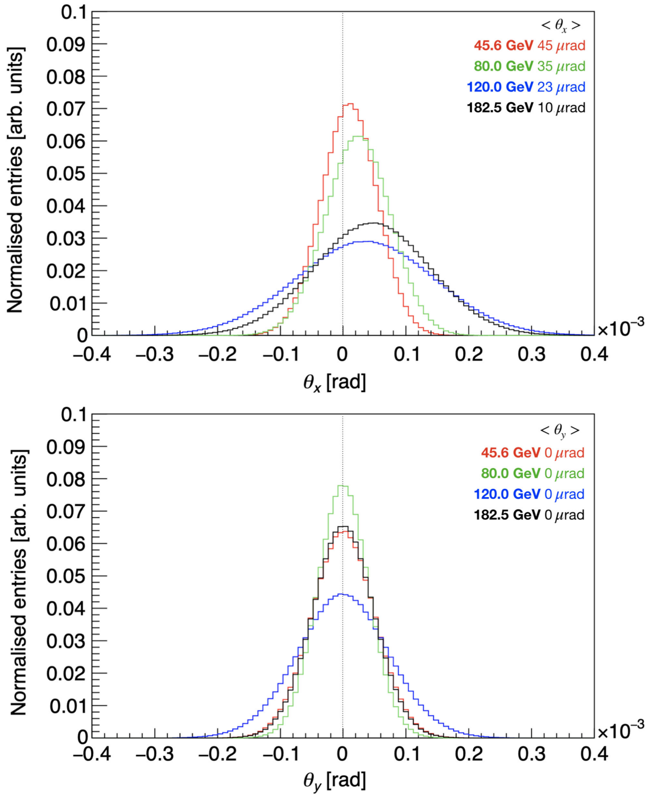

FIG. 2. Horizontal (top) and vertical (bottom) angle distributions of the BS radiation for the four FCC-ee working points.

Figure 3 shows the correlation between the BS photon energy and the horizontal emission angle. The energy of the BS photon depends on the intensity of the beam-beam kick received by the emitting particle. This appears by the green histogram of Fig. 3, which reports the average energy of the photons emitted at a given horizontal angle. If the angular distribution of the BS radiation is weighted by the photon energy, we notice that the center of the power angular distribution is slightly shifted with respect to the geometrical one. The difference between the power and the geometrical angular distribution is about 10 μrad, implying that even at few hundreds meters from the IP, the offset would be about 1 mm for the four working points.

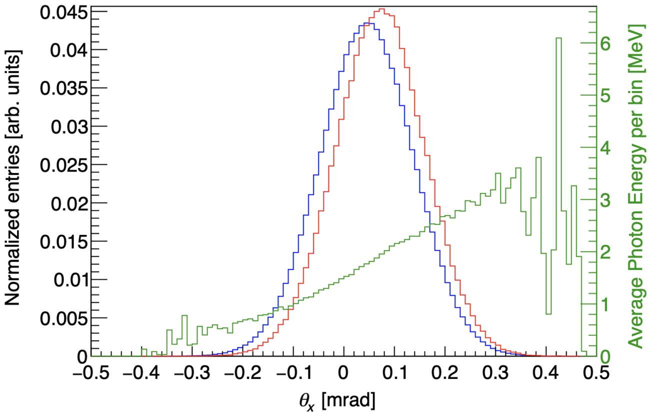

FIG. 3. Comparison of the geometrical (blue) and energy weighted (red) horizontal angular distribution for the BS photons emitted at the Z-pole. In green the average photon energy per each angular bin.

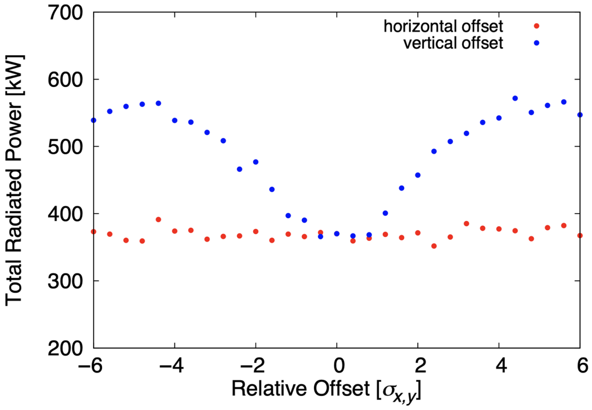

FIG. 4. Total power radiated via BS as a function of the relative horizontal (red) and vertical (blue) offset between the bunches.

Therefore, even applying an offset due to different magnetic rigidity and photon energy distribution, the spots will be mostly overlapping at all beam energies.

The strength of the beam-beam force and the intensity of the BS radiation depend on the charge density distribution of the two beams. We performed a scan on the horizontal and vertical offset between the two opposing bunches.

We considered relative offsets up to $\pm 6\sigma_x^*$ on the horizontal plane and $\pm 6\sigma_y^*$ on the vertical plane. We observe in Fig. 4 that the total power is independent from the horizontal offset, due to the crossing angle and to the long bunch length with respect to σ_x. In the event of two bunches colliding with a vertical offset, the total radiated power at the Z-pole increases to values that exceed 500 kW for lattice v530.

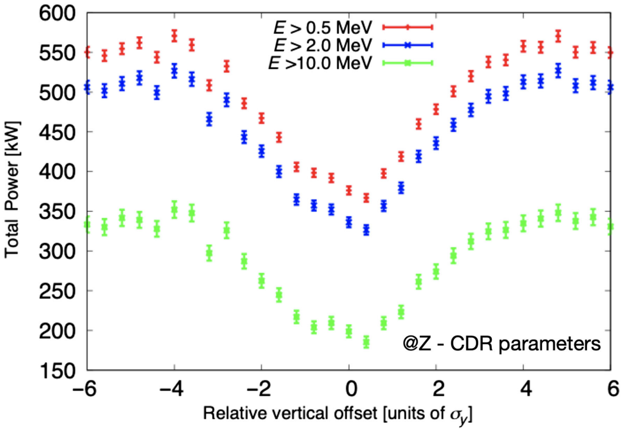

FIG. 5. Total power of the BS radiation as a function of the vertical offset between the colliding beams with beam parameters at the Z-pole. Different energy cuts on the photon energy are shown in red, blue, and green.

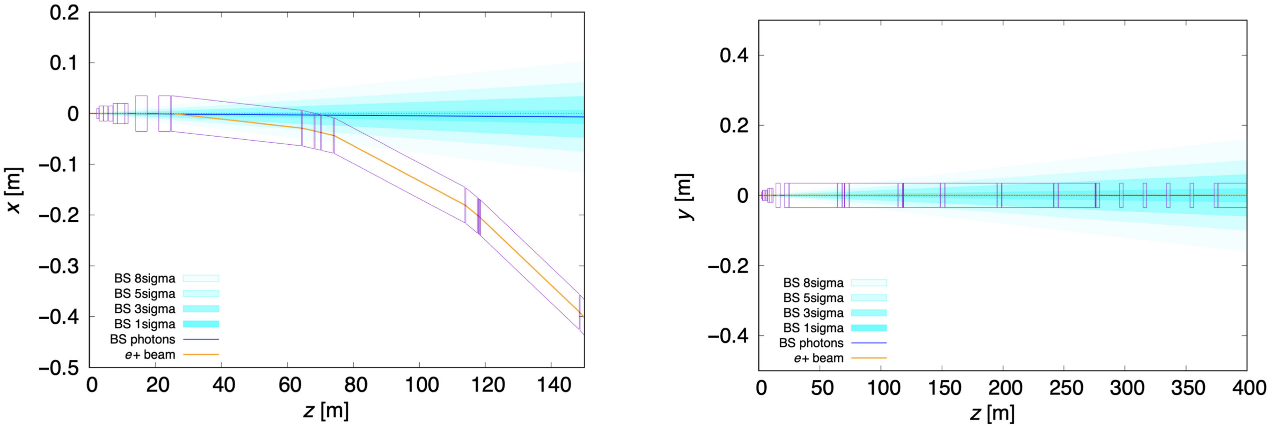

FIG. 6. Left: BS photons path on the x-z plane with respect to the downstream vacuum chamber for the Z-pole c.o.m. energy. Right: corresponding path on the y-z plane.

In Fig. 5 we applied three energy cuts, 0.5, 2.0, and 10 MeV to analyze the photon energy as a function of the vertical offset, shown in red, blue and green curves, respectively. It can be observed that about half of the power is carried by hard photons, in agreement with the definition of the critical energy as for the synchrotron radiation, which is related to the mean photon energy by $E_{\text{crit}} = 15\sqrt{3}/8\langle E\rangle$. E_{crit} is about 7 MeV at the Z-pole.

Figure 5 shows the result of this study at the Z-pole.

IV. BEAMSTRAHLUNG PHOTON BEAM TRAJECTORY

The BS radiation is collinear with the beam, as discussed in Sec. III, so it will hit the vacuum chamber of the first downstream bending magnet (BC1), which is 40 m long and starts about 25 m from the IP, and following elements. Figure 6 shows the photons hitting the internal side of the vacuum chamber for the Z-pole c.o.m. energy case. Although the transverse spot size of the photons is about 1 cm^2, the irradiated region is several meters long due to the angle of incidence of the photons, which is about 1 mrad.

Figure 7 shows the conceptual design of the BS extraction line. First evaluations performed by the magnet experts are encouraging and confirm the possibility to design custom magnets downstream the IP with large aperture yokes to extract the BS radiation from the beam vacuum chamber and transport it to a proper dump [22].

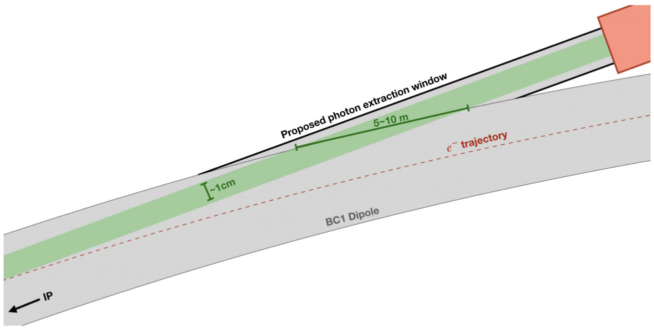

FIG. 7. Conceptual sketch of a BS photon extraction line at the first bending magnet after the IP (not to scale).

Comparing the trajectory of the positron (or electron) beams obtained from MAD-X [23] with that of the BS radiation, we observe that at about 250 m from the IP the two beam lines are at an horizontal distance of 1 m, as shown in Fig. 8. This distance is about the minimum required to position a separate alcove for a BS photon dump. According to these studies, we agreed with the civil engineering group to set the BS dump at about 500 m from the IP [24].

We note that in a 4 IP lattice it will be necessary to have a total of 8 photon extraction lines and beam dumps, two for each IP.

V. DEPENDENCE OF BS RADIATION TO BEAM PARAMETERS AND OPTICS

We have presented the case study for the baseline optics labeled v530. In comparison we also discuss results with

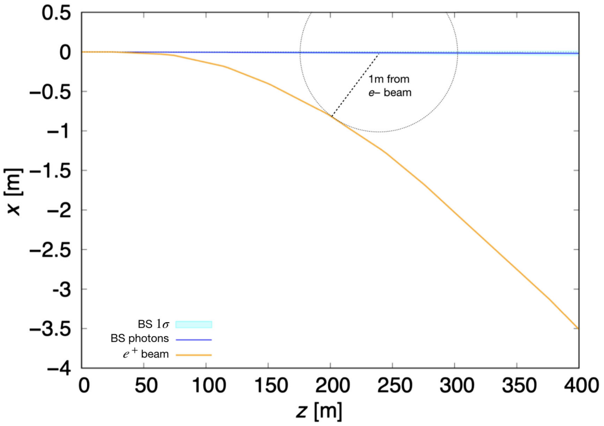

FIG. 8. Trajectory of the electron/positron and BS photon beams. At 250 m after the IP the distance is 1 m.

TABLE IV. BS parameters for v530 [12] and v566 [25] optics.

		N_e (10^{11})	Tot. power (kW)	$\langle E_\gamma \rangle$ (GeV)	$\langle n_\gamma \rangle$ (1)	$\langle \theta_x \rangle$ (μrad)	σ_{θ_x} (μrad)	$\langle \theta_y \rangle$ (μrad)	σ_{θ_y} (μrad)
v530	Z	2.43	370	2	0.16	45	91	0.080	49.2
	WW	2.91	236	7	0.25	35	110	−0.040	73.0
	ZH	2.04	147	22	0.25	23	52	−0.044	41.3
	$t\bar{t}$	2.37	77	62	0.24	10	45	−0.004	50.3
v566	Z	1.51	181	1.5	0.11	30	84	0.036	49.1
	WW	1.47	118	6	0.16	20	107	−0.535	52.0
	ZH	1.15	80	19	0.16	16	57	−0.391	41.3
	$t\bar{t}$	1.55	41	53	0.16	5	43	−0.045	36.4

optics version v566 [25], where the nominal beam current is obtained with a lower number of particles per bunch and a higher number of bunches, relaxing the beam-beam force and, in turn, the BS radiation. The number of photons emitted per particle and their average energy are proportional to the beamstrahlung parameter, which in turns is proportional to the bunch population according to Eqs. (2), (4), and (5). The reduction of the BS power for the optics v566 with respect to that of optics v530 is consistent with the corresponding reduction of the bunch population.

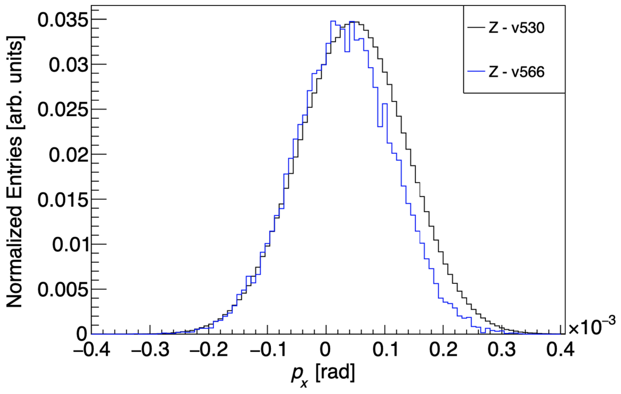

FIG. 9. Photon horizontal angular distribution for v530 and v566 optics at the Z working point.

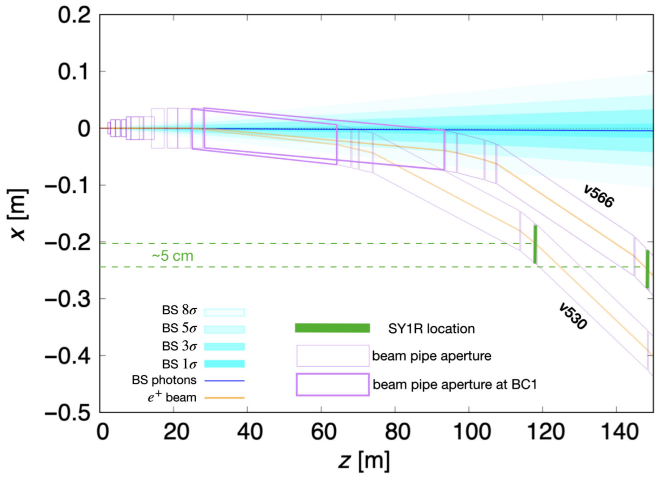

FIG. 10. Comparison of the beam lines after the IP for v530 and v566 optics.

For the optics v566 the lower bunch charge lowers the lower beam-beam kick, and the horizontal angular divergence after the IP, as reported in Table IV. This difference between the two optics is small enough to assure that the core of the two beam distributions are broadly overlapped, as shown in Fig. 9 for the Z-pole energy.

The rms of the angular distributions does not change significantly, because this value is dominated by the divergence of the electron (positron) beam, as discussed in the previous section.

Figure 10 shows the comparison of the two beam lines downstream the IP for the v530 and v566 optics.

For the v566 case the first dipole after the IP (BC1) is much longer than for v530. This modification is relevant for the design of the dipoles between the IP and the BS extraction line. The aperture yokes of the dipoles need to be larger than the BS photon envelope, and the BS photon envelope is strongly dependent on the dipoles location, magnetic length and strength.

VI. PHOTONS FROM RADIATIVE BHABHA SCATTERING

An additional source of radiation coming from the IP is radiative Bhabha (otherwise known as single beamstrahlung). This radiation is emitted in the same radiation cone of about $1/\gamma$ as for the BS, so this radiation will be extracted and collected in the same BS dump.

We used the Monte Carlo generator BBBREM [26] and GuineaPig++ to characterize the radiation emitted via this process at the four FCC-ee working points.

Figure 11 shows the horizontal angular distribution in the downstream beam pipe reference frame for the radiative Bhabha photons at the four FCC-ee working points. The photon mean horizontal angle is inversely proportional to the magnetic rigidity of the beam (i.e., the nominal energy). These values are comparable with those obtained for the BS radiation (Fig. 2), so that the two photon beams will overlap. Table V shows the total power carried by the radiative Bhabha photons, together with the average and rms values of the radiation horizontal angle.

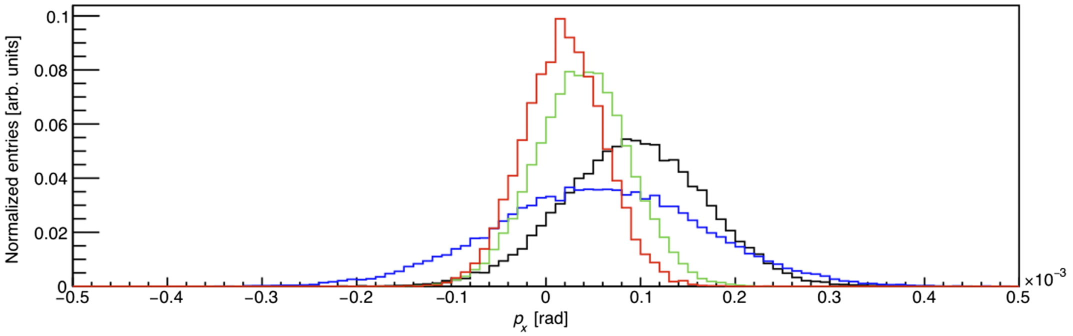

FIG. 11. Radiative Bhabha horizontal angular distribution at the four FCC-ee working points: Z (black), WW (blue), ZH (green), $t\bar{t}$ (red).

Figure 12 shows the energy spectrum of the radiative Bhabha photons at the four FCC-ee working points. Compared to the beamstrahlung energy spectrum (Fig. 1) this radiation is several order of magnitudes less intense, but the endpoint energy of the distribution corresponds to the nominal energy of the beam, while for the beamstrahlung it is few MeV.

In terms of radiated power, the highest value is obtained at the Z-pole for $\mathcal{O}(500W)$, going down to few Watts at the other working points. Therefore the contribution to the deposited power on the beamstrahlung dump due to radiative Bhabha can be considered negligible.

This process has been used in several lepton colliders to provide fast luminosity measurements, like DAΦNE, VEPP, PEP-II, [27–29]. The possibility to use radiative Bhabhas for relative luminosity measurements for machine tuning is being considered. The challenge here is to be able to discriminate radiative Bhabhas from BS photons as well as SR.

VII. BEAMSTRAHLUNG INDUCED DETECTOR BACKGROUNDS

The beamstrahlung radiation is produced in the direction of the outgoing beams and does not directly hit the detector. However, the interaction of the beamstrahlung photons with other real or virtual photons at the IP can be the source of e^+e^- pairs emitted at large angles, which can enter the detector and cause background. This process is known as incoherent pair creation (IPC) [4].

TABLE V. Divergence of the radiative Bhabha photon beam at the four working points.

	P_{tot} (W)	$\langle\theta_x\rangle$ (μrad)	σ_{θ_x} (μrad)
Z	430	93	76
WW	60	56	109
ZH	40	39	50
$t\bar{t}$	2	19	43

Figure 13 shows the production kinematics of these particles for the Z and $t\bar{t}$ working points at FCC-ee. Most of the high-energy particles are produced at an angle of $\theta = 0.015$ rad in the detector reference frame. This value means that these particles are emitted collinearly with the beam.

For $p_T < 100$ MeV two distinct particle families can be identified according to their deflection angle. Particles emitted in the direction of the beam with the opposite charge (e.g., a positron from the pair emitted in the direction of the outgoing electron beam) will experience a focusing force due to the electric field and will populate the two branches at low θ visible in Fig. 13. On the other hand, particles emitted in the direction of the beam with the same charge (e.g., a positron from the pair emitted in the direction of the outgoing positron beam) will experience a defocusing force and will be deflected to large angles.

These particles can enter the acceptance of the innermost subdetectors and be the source of background. To evaluate the level of this background, the IPC particles have been tracked in the CLD detector model [30] using Key4HEP. In particular, the occupancy in the vertex detector (VXD) and inner/outer trackers (TRK) has been studied. The model description of the VXD barrel has been modified after the CDR since the study described in Ref. [30], following the

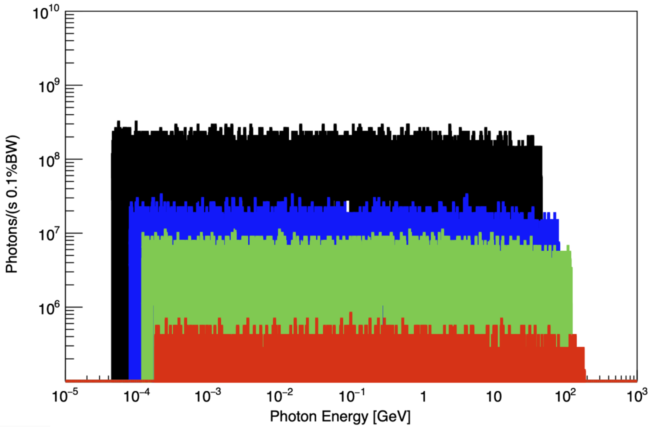

FIG. 12. Radiative Bhabha energy spectrum at the four FCC-ee working points: Z (black), WW (blue), ZH (green), $t\bar{t}$ (red).

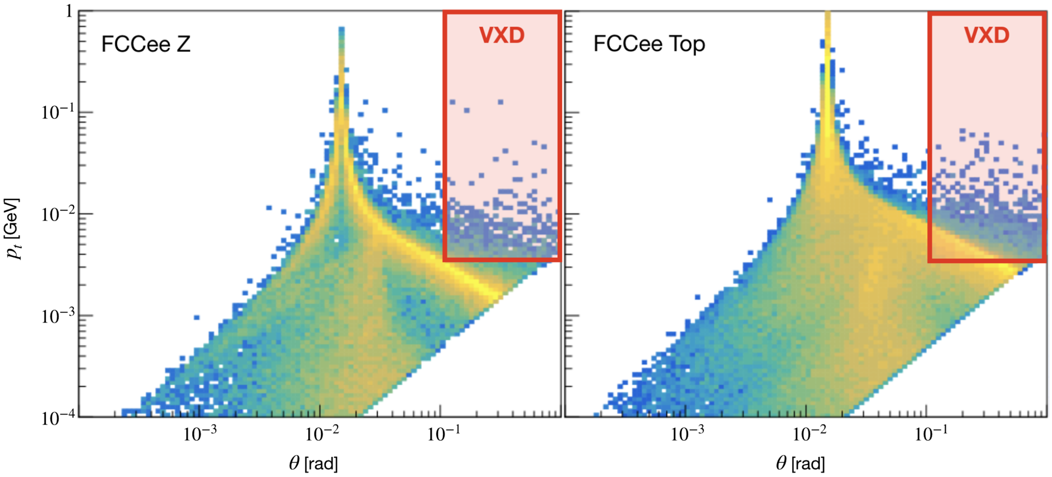

FIG. 13. Production kinematics of the IPC particles emitted at FCC-ee for the Z and top working points. The red area represents the acceptance of the CLD vertex detector (VXD).

reduction of the smaller central vacuum chamber from 15 to 10 mm. The occupancy is defined as:

$$\text{Occupancy} = \mathrm{HD}_{\mathrm{BX}} \times S_{\mathrm{size}} \times C_{\mathrm{size}} \times S_{\mathrm{factor}}, \qquad (10)$$

where $\mathrm{HD}_{\mathrm{BX}}$ is the hit density per bunch crossing (expressed in hits/mm^2/BX), S_{size} is the sensor size (25 μm × 25 μm for the VXD silicon pixels, and 1 mm × 0.05 mm for the TRK strips), C_{size} is the cluster size (5 for the pixels and 2.5 for the strips), and S_{factor} is a safety factor to account for uncertainties on the simulation of detector materials effects (e.g., backscattering), which for this study has been set to 3.

In a silicon detector, the occupancy is the number of channels that have signal above threshold. To account for this, a cut on the energy deposited in the detectors has been set to 4 keV for the VXD and 8 keV for the TRK.

Table VI summarizes the results of the study conducted for the four FCC-ee working points. The number of e^+e^- pairs produced increases proportionally with the beam energy, as expected from the cross section. The maximum occupancy recorded for each subdetector is also larger at higher energies, but in particular for the vertex detector barrel it grows more rapidly with respect to the total number of pairs. This can be explained with the fact that a larger fraction of the particles is produced inside the acceptance of the VXD at higher energies, as highlighted by the red area in Fig. 13.

The detector group poses a constraint to the allowable occupancy, set to a limit of about 1%. Table VI shows that in no subdetector the occupancy exceeds this safety value, even when accounting for the possibility of pileup in a hypothetical electronics readout window of 1 μs.

The arrival time of the particles at the innermost subdetectors of the CLD vertex detector and inner tracker (IT) is shown on the left side of Fig. 14. The position of these elements is shown in the right side of Fig. 14, respectively, VXD Barrel Layer 1 (VXDB L1: red), VXD Endcap Disk 1 (VXDE D1: green), IT Barrel Layer 1 (ITB L1: blue), IT Endcap Disk 1 (ITE D1: magenta). The first peak in the arrival time distribution corresponds to particles traveling straight from the IP to the

TABLE VI. Pairs produced per bunch crossing at the four FCC-ee working points and maximum occupancy in the VXD and TRK subdetectors of CLD, also considering the pileup effect in two arbitrary readout time windows of 1 μs and 10 μs.

	Z	WW	ZH	Top
Pairs produced per Bunch Crossing	1300	1800	2700	3300
Max occupancy VXD Barrel	70×10^{-6}	280×10^{-6}	410×10^{-6}	1150×10^{-6}
Max occupancy VXD Endcap	23×10^{-6}	95×10^{-6}	140×10^{-6}	220×10^{-6}
Max occupancy TRK Barrel	9×10^{-6}	20×10^{-6}	38×10^{-6}	40×10^{-6}
Max occupancy TRK Endcap	110×10^{-6}	150×10^{-6}	230×10^{-6}	290×10^{-6}
Bunch Spacing (ns)	30	345	1225	7598
Max occ. VXD w/1 μs pileup	2.33×10^{-3}	0.81×10^{-3}	410×10^{-6}	1150×10^{-6}
Max occ. VXD w/10 μs pileup	23.3×10^{-3}	8.12×10^{-3}	3.34×10^{-3}	1.51×10^{-3}

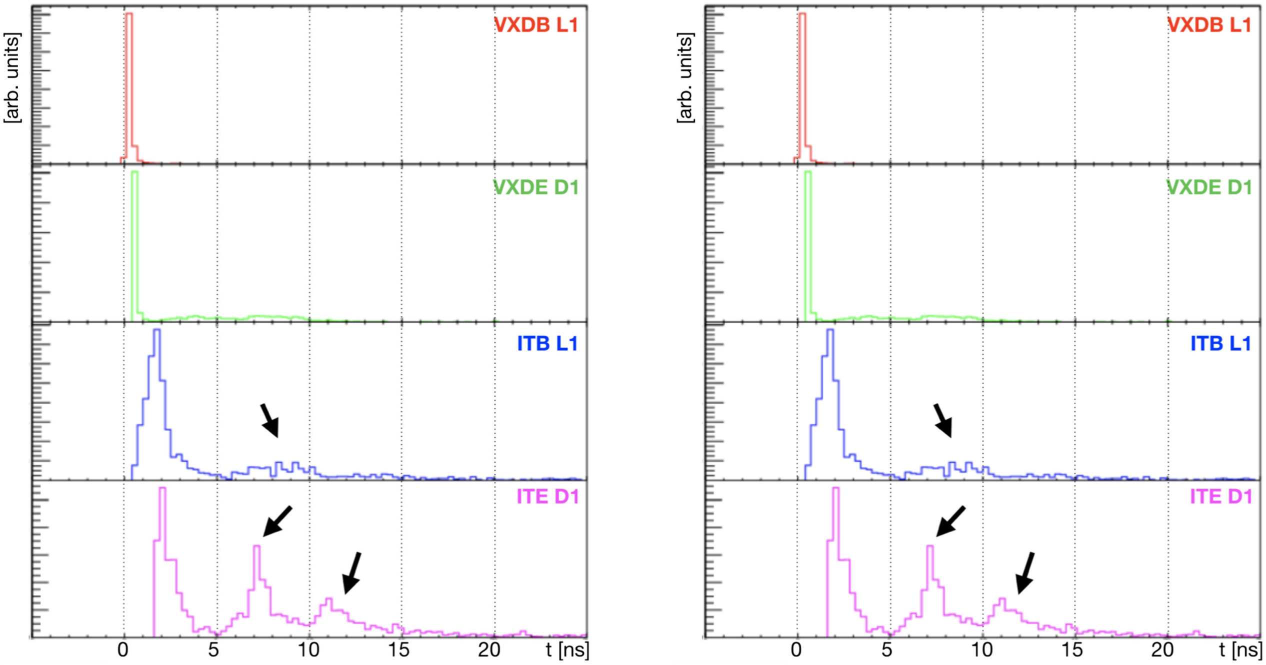

FIG. 14. Left: arrival time of the particles in the subdetectors. Right: Position of the considered subdetectors: VXDB L1 (red), VXDE D1 (green), ITB L1 (blue), ITE D1 (magenta).

detector but, in particular for the inner tracker, secondary peaks can be observed after the first one. These can be explained as a contribution from backscattered particles. This signal could be rejected offline, further reducing the background induced by the IPC.

A consideration that should be done by looking at Eq. (10) is that it strongly depends on the sensor and cluster size. While for a Silicon based detector these values, in particular the sensor size, can be very small, they can be much larger for other types of detectors (e.g., drift chambers, wire chambers, …) and the same background source can be negligible for a detector but relevant for another. Therefore it is important to repeat these studies for the other experiment proposals for FCC-ee.

VIII. CONCLUSION

We have discussed the properties of the beamstrahlung radiation emitted in a single beam-beam interaction for the FCC-ee collider, showing that we estimate an intense power of about 500 kW for the baseline optics labeled v530. A relevant reduction of this BS power is found with a different beam parameter set and different optics labeled v566; we have shown that the dominant parameter for the BS power is the reduction of the bunch population, that brings, on the other hand, a lower luminosity. For this reason a trade-off between all the beam parameters is still in progress together with the optics optimization. We showed that the beamstrahlung photons hit the vacuum chamber inside the first dipole magnet downstream the IP, at about 60 m from the IP. This results is the basis for the design of a dedicated extraction line to transport the beamstrahlung radiation up to a photon beam dump. Based on these first evaluations, detailed FLUKA simulations and dedicated study to design the magnets and beam pipe for the extraction line are planned, to develop a concept for the photon beam dump including the proper target material and finally to design the alcove for the dump. This work is part of the FCC-ee MDI study group.

We have described the induced backgrounds in the CLD detector due to beamstrahlung radiation. Detector backgrounds simulations show that the occupancy in the CLD Silicon vertex and tracker detectors due to the incoherent pairs produced by the beamstrahlung photons at the IP is below the safety value set by the detector group of 1%, also accounting for hypothetical pileup effects. The analysis of the background particles arrival time showed a non-negligible contribution coming from backscattering, which could be removed offline further reducing the noise. We plan to repeat the study for the other FCC-ee detectors, as different detector technologies can significantly affect the final occupancy.

ACKNOWLEDGMENTS

The authors would like to thank the colleagues from the MDI group for useful discussions, in particular Helmut Burkhardt, Anton Lechner, Emmanuel Francois Perez, Dmitry Shatilov, and Katsunobu Oide. This work was partially supported by the European Union's Horizon 2020 research and innovation programme under Grant No. 951754 - FCCIS Project.

The authors declare that they have no competing interests.

[1] A. Abada *et al.* (FCC Collaboration), FCC-ee: The Lepton Collider: Future Circular Collider conceptual design report volume 2, Eur. Phys. J. ST **228**, 261 (2019).

[2] A. Hofmann and E. Keil, Synchrotron radiation caused by the field of the other beam, CERN Report No. CERN-LEP-70/86, 1978, https://cds.cern.ch/record/443445.

[3] J. Augustin *et al.*, Limitations on performance of e^+e^- storage rings and linear colliding beam systems at high energy, Report No. PLAD-1978-009, 1978, https://inspirehep.net/literature/138170.

[4] K. Yokoya and P. Chen, Beam-beam phenomena in linear colliders, Lect. Notes Phys. **400**, 415 (1992).

[5] P. Chen, The nature of beamstrahlung, SLAC Report No. SLAC-PUB-4293, 1987, https://inspirehep.net/literature/246495.

[6] D. Schulte, Beam-beam simulations with GUINEA-PIG, CERN Report No. CERN-PS-99-014-LP, 1999, http://cds.cern.ch/record/382453.

[7] G. Ganis *et al.*, Key4hep, a framework for future HEP experiments and its use in FCC, arXiv:2111.09874.

[8] M. Sands, The physics of electron storage rings: An introduction, Conf. Proc. C **6906161**, 257 (1969), SLAC-R-121, https://inspirehep.net/literature/60854.

[9] A. Bogomyagkov, E. Levichev, and D. Shatilov, Beam-beam effects investigation and parameters optimization for a circular e^+e^- collider at very high energies, Phys. Rev. ST Accel. Beams **17**, 041004 (2014).

[10] M. A. V. García and F. Zimmermann, Effect of beamstrahlung on bunch length and emittance in future circular e^+e^- colliders, in *Proceedings of International Particle Accelerator Conference, IPAC2016, Busan, Korea* (JACoW, Geneva, 2016), WEPMW010.

[11] D. Shatilov *et al.*, Lifetrac code for the weak-strong simulation of the beam-beam effects in Tevatron, in *Proceedings of the 21st IEEE Particle Accelerator Conference, Knoxville, TN, USA, 2005*, p. 4138, https://inspirehep.net/literature/687566.

[12] K. Oide, Collider Optics. FCCIS 2022 Workshop, https://indico.cern.ch/event/1203316/contributions/5125285/.

[13] T. Barklow *et al.*, Experimental evidence for beam-beam disruption at the SLC, SLAC Report No. SLAC-PUB-8043, 1999.

[14] G. Aarons, International linear collider reference design report, 2007, 10.2172/929487.

[15] M. Aicheler *et al.*, The Compact Linear Collider (CLIC)—Project Implementation Plan, CERN Yellow Reports: Monographs, Vol. **4/2018**, CERN-2018-010-M, 10.23731/CYRM-2018-004

[16] T. Raubenheimer *et al.*, Parameters of the SLAC Next Linear Collider, 10.1109/PAC.1995.504762

[17] K. Akai *et al.*, SuperKEKB Collider, arXiv:1809.01958v2.

[18] M. Zobov *et al.*, Test of “crab-waist” collisions at the DAΦNE Φ-factory, Phys. Rev. Lett. **104**, 174801 (2010).

[19] M. A. V. García and F. Zimmermann, Beam blow up due to beamstrahlung in circular e^+e^- colliders, Eur. Phys. J. Plus **136**, 501 (2021), .

[20] H. Burkhardt, Radiation generated at the IP, FCC-ee optics design meeting #105, https://indico.cern.ch/event/854159/.

[21] M. Boscolo, N. Bacchetta, M. Benedikt, L. Brunetti, H. Burkhardt, A. Ciarma, M. Dam, F. Fransesini, M. Jones and R. Kersevan *et al.*, Challenges for the interaction region design of the Future Circular Collider FCC-ee, 10.18429/JACoW-IPAC2021-WEPAB029.

[22] C. J. Eriksson and J. Bauche, Magnet design for beamstrahlung photons extraction line, FCC-ee MDI meeting #43 and FCCIS WP2.3 meeting #14, https://indico.cern.ch/event/1241377/.

[23] MAD-X, Methodical Accelerator Design, http://mad.web.cern.ch/mad.

[24] F. Valchkova-Georgieva, Tunnel integration, FCCIS 2022 Workshop, https://indico.cern.ch/event/1203316/contributions/5125332/.

[25] K. Oide, Layout, optics, parameters, FCCWeek 2023, London, https://indico.cern.ch/event/1202105/contributions/5408583/.

[26] R. Kleiss and H. Burkhardt, BBBREM—Monte Carlo simulation of radiative Bhabha scattering in the very forward direction, CERN Report No. SL/94-03, 1994.

[27] M. Greco, G. Montagna, O. Nicrosini, and F. Piccinini, Radiative Bhabha scattering at DAΦNE, Phys. Lett. B **318**, 635 (1993).

[28] A. E. Blinov, A. E. Bondar, A. D. Bukin, S. G. Klimenko, G. M. Kolachev, A. P. Onuchin, A. G. Shamov, V. I. Telnov, Yu. A. Tikhonov, and V. N. Zhilich, Luminosity measurement with the MD-1 detector at VEPP-4, Nucl. Instrum. Methods Phys. Res., Sect. A **273**, 31 (1988).

[29] S. Ecklund, C. Field, and G. Mazaheri, A fast luminosity monitor system for PEP II, SLAC Report No. SLAC-PUB-8688, 2000.

[30] N. Bacchetta *et al.*, CLD—A detector concept for FCC-ee, arXiv:1911.12230.